Contrib Mineral Petrol (2014) 167:1000
DOI 10.1007/s00410-014-1000-z

ORIGINAL PAPER

Zircon trace element chemistry at sub-micrometer resolution for Tarawera volcano, New Zealand, and implications for rhyolite magma evolution

Sonja Storm · Axel K. Schmitt ·
Phil Shane · Jan M. Lindsay

Received: 4 December 2013 / Accepted: 18 March 2014 / Published online: 2 April 2014

Abstract Zoned crystals can be important recorders of magmatic processes in space and time. However, in most situations, the temporal dimension is difficult to quantify. Here, we have employed secondary ion mass spectrometry depth profiling to excavate parallel pits into non-polished crystal faces of zircon to obtain ~5 μm resolution U–Th disequilibrium ages (one pit) that can be correlated with trace element zoning at sub-μm resolution derived from a second pit. Data from 17 crystals representing each of the four rhyolite eruptions of Tarawera volcano, an intra-caldera edifice within the Okataina Volcanic Centre, reveal diverse zircon growth conditions over time. Most crystals display rimward depletions in Zr/Hf and Ti, broadly consistent with cooling and crystallization. However, a significant fraction of crystals lacks these patterns and displays rimward trace element variations consistent with isothermal or prograde crystallization. Oscillatory zonation patterns in Y, Th, and U are superimposed on the Zr/Hf and Ti trends. Despite the limited number of crystals analyzed in this way, the striking lack of ubiquitous trace element zoning patterns in crystals from the same hand sample implies that fractional crystallization upon cooling was punctuated by magma recharge and crystal mixing affecting different parts of the magma reservoir. By combining data from all crystals, a systematic change to more heterogeneous trace element abundances is revealed by zircon crystal domains <45 ka following the Rotoiti caldera-forming eruption. This contrasts with the more uniform conditions of zircon crystallization lasting >100 ka prior to caldera formation and is best explained by the post-caldera system consisting of small, isolated melt pockets that evolved independently. An important conclusion is that the zircon 'cargo' in volcanic rocks reflects thermally and compositionally divergent processes that act near simultaneously in a magma storage region and not exclusively the conditions in the eruptible magma.

Keywords Zircon · Geochronology · Geothermometry · Caldera · Secondary ionization mass spectrometry

Introduction

Silicic magmatism is a fundamental process in the evolution of continental crust, but the physical nature and timescales over which eruptible magma resides in shallow crustal magma reservoirs remain debated. The Okataina Volcanic Centre (OVC) in New Zealand (Fig. 1) has erupted rhyolite approximately every 1–4 ka for the last 45 ka, thus providing a frequent yet punctuated record of eruptible magma that has been used to reconstruct pre-eruptive storage conditions in voluminous silicic magma reservoirs (e.g., Nairn 2002; Shane et al. 2008a, b; Shane and Smith 2013). Compositional zoning in volcanic minerals can reveal the physicochemical conditions in magma over various timeframes under which they crystallized

---

Communicated by J. Hoefs.

Electronic supplementary material The online version of this article (doi:10.1007/s00410-014-1000-z) contains supplementary material, which is available to authorized users.

S. Storm · P. Shane · J. M. Lindsay
School of Environment, University of Auckland,
Private Bag 92019, Auckland 1142, New Zealand

A. K. Schmitt (✉)
Department of Earth, Planetary, and Space Sciences, University of California Los Angeles, 595 Charles Young Drive E,
Los Angeles, CA 90095, USA
e-mail: axel@argon.ess.ucla.edu; axel@oro.ess.ucla.edu

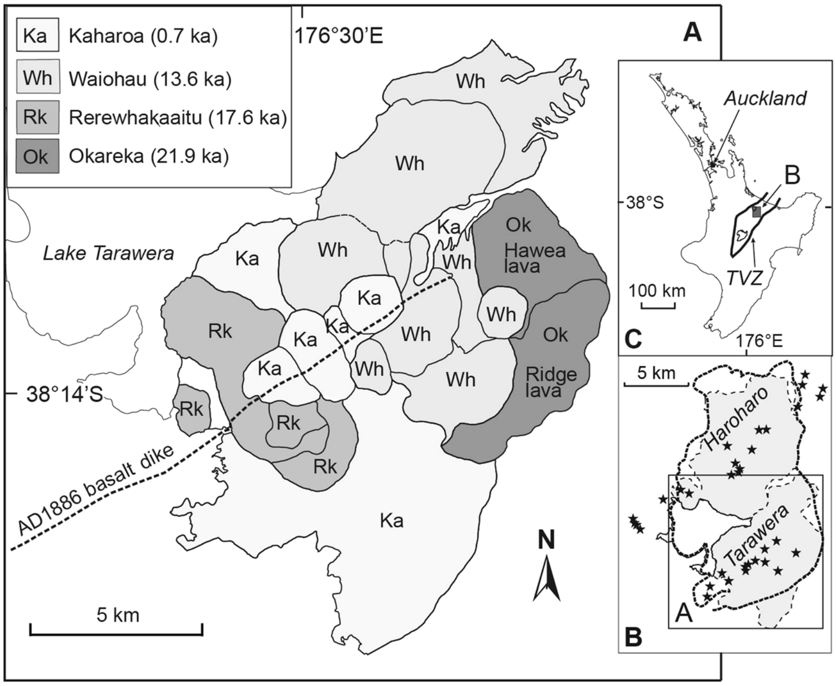

Fig. 1 **a** Map of Tarawera volcano showing lava domes and pyroclastic units from the four rhyolite eruption episodes (modified from Nairn 2002). **b** Map of the OVC showing Tarawera and Haroharo volcanic complexes. *Stars* mark rhyolite vents active during the last 25 ka. **c** Map of the North Island of New Zealand showing the location of the TVZ

(e.g., Ginibre et al. 2007; Davidson et al. 2007). Hence, individual crystals can provide a quasi-continuous record of magmatic evolution and permit insights into the conditions of magma accumulation and storage and how this relates to volcanic activity. However, the time over which compositional zonation developed is often difficult to constrain because of (1) the small dimensions (micron-scale) of the growth domains; (2) diffusive redistribution of components between crystal domains, or crystal resorption; and (3) lack of absolute or relative dates on crystal growth. Zircon offers unique insights into the timing of magmatic processes because it permits absolute dating of magmatic crystallization and its diffusive robustness preserves delicate growth domains whose variability in trace element abundances is often visible in cathodoluminescence (CL) imaging (Watson 1996; Cherniak and Watson 2003; Schmitt 2011; Schmitt et al. 2011; Storm et al. 2012). Presently, the only technique with a temporal resolution at a millennial-scale commensurate to the spatial dimensions of individual zircon growth domains is U-series disequilibrium (^{230}Th/^{238}U) geochronology determined by ion microprobe techniques (e.g., Reid et al. 1997).

Tarawera volcano is one of the youngest volcanoes of the OVC, and its dominantly rhyolitic eruptions have produced zircon crystals which record protracted but intermittent crystallization over the lifetime of the OVC and its precursors (Storm et al. 2011; 2012; Shane et al. 2012). This provides an opportunity to compare chemical records within long-lived zircon crystals with those of erupted magmas within a well-constrained temporal framework. Taking this approach was first attempted for the OVC by Klemetti et al. (2011). Here, we introduce an alternative analytical strategy based on continuous zircon depth profiling (e.g., Reid and Coath 2000), concentrating on the analysis of trace element abundances in zircon that are directly (Ti in zircon) or indirectly (Zr/Hf) indicative of magmatic temperature and thus of the physicochemical conditions in the magma (e.g., Ferry and Watson 2007; Claiborne et al. 2006). This not only enables us to quantify elemental distributions and to compare them with patterns visible in CL imaging, but also to quantitatively co-register zircon trace element- and age-depth profiles in the same crystals. As a result, we can complement whole-rock data from punctuated eruptions with the quasi-continuous crystal record to monitor the chemical and physical conditions in a rhyolitic magma system.

Zircon micro-sampling strategies

Micro-beam analysis of zircon is conventionally performed on cross-sectioned crystals with the plane of sectioning typically parallel to the crystal's *c*-axis (e.g., Reid et al. 1997). Electron beam imaging (e.g., CL) can reveal the internal structure of the crystals at a spatial resolution of ~1 µm, and electron probe microanalysis (EMPA) has the sensitivity to detect distributions of some trace elements such as Y and Hf in zircon (Klemetti et al. 2011). However, electron beam techniques lack the sensitivity to detect low-abundance trace elements such as Ti. Isotope-selective,

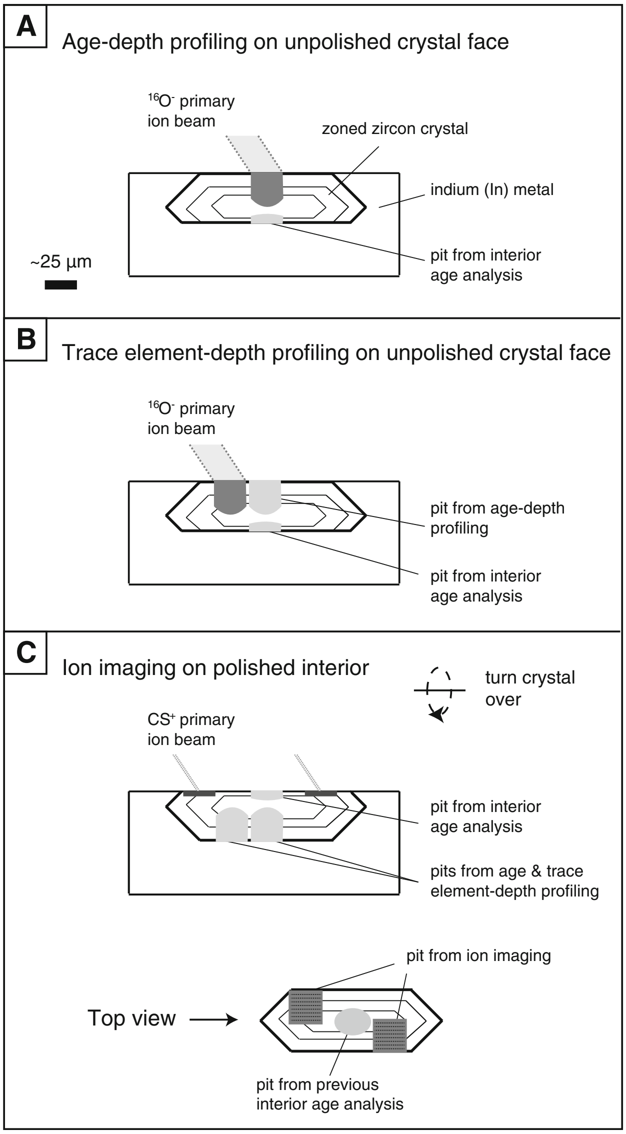

Fig. 2 Schematic sketch illustrating the micro-sampling techniques for zircon dating and trace element analyses by SIMS used in this study. **a** The zircon crystal that was first sectioned and analyzed for its interior age is turned over 180° and pressed into soft indium (In) metal with the crystal face flush to the mount surface. The age-depth profile is then drilled from the non-polished surface toward the interior, providing a continuous age record of the zircon's crystallization history (Storm et al. 2011, 2012). **b** In order to enable the correlation between the zircon's composition and its crystallization ages, the trace element depth profile is drilled directly adjacent to the age profile. **c** The 2D distribution of trace elements is investigated by ion imaging. For this, the crystal is extracted from the mount, turned over 180°, and imbedded so that the previously polished section with the pit from the interior age analysis is flush with the mount surface again. The ion images are analyzed in areas of the crystal that show distinct CL zoning

high-sensitivity secondary ion mass spectrometry (SIMS) is required for dating crystal domains and for determining low-abundance trace elements. Typically employed lateral beam dimensions in SIMS (~10–30 µm) in conventional spot analysis mode preclude analysis of individual chemical zones in zircon. To correlate EMPA, chemical analysis with SIMS geochronology thus requires assumptions regarding the age of those crystal domains that are too small to be directly accessible for dating (e.g., Klemetti et al. 2011).

To overcome these limitations, we utilize the superior depth resolution of SIMS which is at least one order of magnitude smaller than its lateral beam dimensions. For zircon, we apply 'depth-profiling' analyses where crystal growth domains are sequentially intersected by the ion beam which is targeted perpendicular to the (100) or (110) prism faces mounted parallel to the surface of the analysis mount (Fig. 2). Practical limitations regarding the switching of magnetic fields at high mass resolution during SIMS analyses led us to conduct two parallel depth profiles: one for U-series disequilibrium and one for trace elements. To correlate both profiles, we use U and Th abundances, which were determined in both profiles. To allow for high spatial resolution ion beam imaging of the zircons' interior structures, trace element depth profiles were carried out after the following steps: (1) analysis of non-polished crystals to determine 'rim' crystallization ages; (2) grinding and polishing to expose interiors which were then CL imaged; (3) spot analysis of sectioned crystals which yielded 'interior' ages; (4) rotating sectioned crystals (typically the remaining 2/3 of the crystal) by 180°, exposing a pristine prism face parallel to the plane of sectioning; and (5) conducting two parallel depth profiles (one for U–Th isotopes and the second for selected trace elements) on the pristine crystal face opposite to the ground and polished interior (Fig. 2).

We also selected sectioned crystals and analyzed Ti and Y abundances by secondary ion imaging using a focused Cs^+ ion beam (Harrison and Schmitt 2007). Secondary ion imaging was performed to assess the two-dimensional (2D) distribution of these elements and any potential correlations between CL banding and trace element abundances. It has been previously postulated through ion imaging of Hadean zircon crystals that Ti variations in zircon may not be suitable as temperature indicators if Ti partitioning was affected by ionic substitution and defects in the crystal structure (Hofmann et al. 2009). Because of the long integration time per image (~4–6 h), we tested for potential correlations between Y and Ti as a reconnaissance on four domains with strong CL contrasts of two selected Tarawera zircon crystals.

Geologic background

Okataina Volcanic Centre is part of the Quaternary Taupo Volcanic Zone in New Zealand (Fig. 1), an actively rifting on-land continuation of the Tonga–Kermadec arc, formed at the convergent plate boundary between the westerly subducting Pacific plate and the partly continental Australian plate (e.g., Wilson et al. 2009). OVC eruptions are mostly rhyolitic, and the last major caldera collapse occurred at ~45 ka (Danišík et al. 2012). This event is associated with the Rotoiti pyroclastic deposits comprising >100 km^3 of non-welded ignimbrite and intercalated fall-out deposits (Nairn 2002; Shane et al. 2005a) and is responsible for much of the present morphology of the OVC. Immediately following the Rotoiti event, the Earthquake Flat eruption produced ~10 km^3 of non-welded ignimbrite and tephra fall-out deposits to the southwest of the OVC (Nairn and Kohn 1973; Danišík et al. 2012). Intra-caldera volcanism started with the emplacement of the Mangaone subgroup (>30 km^3 of magma) comprising silicic tephra and ignimbrites erupted in 14 dominantly plinian episodes between 43 and 31.5 ka (Jurado-Chichay and Walker 2000). During the last ~26 ka, nine eruptive episodes built up two sub-parallel northeast trending intra-caldera dome complexes, Haroharo and Tarawera, composed of lavas and pyroclastic deposits with a magma volume of >85 km^3 (Fig. 1; Nairn 2002).

The Tarawera volcanic massif formed during four rhyolite eruptive episodes (~30 km^3 of magma) occurring at 21.9 (Okareka), 17.7 (Rerewhakaaitu), 13.7 (Waiohau), and 0.7 ka (Kaharoa) (ages from Lowe et al. 2008) and one entirely basaltic eruption in AD1886 (Nairn 2002) (Fig. 1). Each rhyolite episode involved the emplacement of pyroclastic fall and flow deposits by sub-plinian to plinian-style activity and the extrusion of lava domes from one or more vents (Nairn 2002). Each of the four rhyolite episodes shows evidence for the eruption of minor amounts of basalt, suggesting basalt intrusion as the eruption trigger mechanism (Shane et al. 2008b).

Tarawera rhyolites have high silica contents (whole rock: 73–77 %) and a mineral assemblage comprising quartz, plagioclase, orthopyroxene, and hornblende (with cummingtonite and biotite in some cases), and spinel, ilmenite, apatite, and zircon as accessory phases (Shane et al. 2008b). During each episode except the 13.7 ka Waiohau event, two or three distinct rhyolite magma types co-erupted. These magma types differ geochemically and by their intensive parameters, ferromagnesian mineral assemblage, and crystallinity (Speed et al. 2002; Nairn et al. 2004; Shane et al. 2007, 2008a) and lack coherent trends that would suggest they were derived from a common melt via fractional crystallization in a closed system (Shane et al. 2008b).

The timing of rhyolite evolution at Tarawera is further constrained by zircon geochronology (Storm et al. 2011, 2012; Klemetti et al. 2011). U–Th zircon ages reveal protracted zircon growth which can predate the eruption by >100 ka. Some zircons indicate cessation of crystallization long before eruption, and others reveal internal growth hiatuses lasting up to 40 ka (Storm et al. 2011, 2012). This points to limited inter-connectivity of the magma system and significant crystal transport and mixing before eruption.

Analytical conditions

Zircon crystals ($n = 244$) from seven samples representing distinct magmas from each of the four Tarawera rhyolite eruptions (Table 1) have been previously analyzed by U–Th geochronology via SIMS (Storm et al. 2011, 2012). Here, we selected a subset of 17 crystals (CL images in Electronic Supplementary Material) with published geochronological data (Storm et al. 2012). These 17 crystals show evidence for protracted crystallization based on U–Th ages ranging between ~5 and ~150 ka which in many cases significantly predate the 21.9–0.7 ka eruption ages (Storm et al. 2012). Trace element depth profiles were acquired for Ti, Hf, Y, Ce, U, and Th. These elements were selected because they are directly and indirectly associated with temperature and degree of crystallization. Translating Ti abundance into Ti-in-zircon temperature (T_{Tiz}) requires constraints on melt Ti activity ($a_{\mathrm{TiO_2}}$), Si activity ($a_{\mathrm{SiO_2}}$), and pressure (P) (e.g., Ferry and Watson 2007) which are detailed below. We report Zr/Hf ratios instead of Hf abundances because this ratio is directly proportional to measured Zr and Hf ion abundances, and it is preferable to Hf concentration because Zr in zircon varies due to substitution by Hf (and other trace elements) in zircon's octahedral site. Zr/Hf is indirectly related to temperature because Zr and Hf are essentially only effectively fractionated by zircon crystallization whose saturation is controlled by the solubility of Zr in the melt. Zr solubility is a function of a melt composition parameter ($M = [\mathrm{Na} + \mathrm{K} + 2 \times \mathrm{Ca}]/[\mathrm{Al} \times \mathrm{Si}]$ as molar abundances) and temperature (Watson and Harrison 1983; Boehnke et al. 2013). The other trace elements analyzed here (Y, Ce, Th, U) are moderately to highly compatible in zircon with mineral-melt partition coefficients (D) between ~1 (D_{Ce}) and ~100 (D_{Y}; D_{U}) (e.g., Blundy and Wood 2003; Reid et al. 2011), but otherwise incompatible in major crystal phases and thus should become enriched in the melt with increasing fractionation.

Zircon trace element abundances were acquired using the UCLA CAMECA ims1270 ion probe (SIMS) by sequentially recording secondary ion intensities for $^{91}\mathrm{Zr}^{++}$, $^{49}\mathrm{Ti}^{+}$, $^{177}\mathrm{Hf}^{++}$, $^{89}\mathrm{Y}^{+}$, $^{140}\mathrm{Ce}^{+}$, $^{178}\mathrm{Hf}^{+}$, $^{180}\mathrm{HfO}^{+}$, $^{197}\mathrm{Au}^{+}$, $^{94}\mathrm{Zr_2O}^{+}$, Th^{+}, and U^{+} using an axial electron multiplier. Secondary ions were generated by bombarding the sample surface with a mass-filtered $^{16}\mathrm{O}^{-}$ primary

Table 1 Samples used for zircon trace element analyses (Storm et al. 2011, 2012). Eruption ages from Lowe et al. (2008)

Sample	Eruption	Magma	Age (ka)	Eruption Unit	Lithology	Grid ref
T005Ka	Kaharoa (Ka)	T2	0.7	Wahanga block/ash flow	Lava block	217291
T014Ka	Kaharoa (Ka)	T1	”	Fall unit F, G	Multiple lapilli	174196
T008Wh	Waiohau (Wh)		13.7	Pokohu Lava	Lava block	202321
T012Rk	Rerewhakaaitu (Rk)	T1, T2	17.7	Fall unit H	Multiple lapilli	238270
T011Ok	Okareka (Ok)	T3	21.9	Hawea lava	Lava block	238270
T018Ok	Okareka (Ok)	T1	”	Fall units B, C	Multiple lapilli	285265

Grid references from Topographic Map 260-V16 Tarawera, Geodetic Datum 1949, New Zealand Map Grid

ion beam at a current of ~60 nA focused into a 25 × 30 µm oval spot. The secondary ion accelerating voltage was 10 kV, and secondary ions with an energy bandpass of 50 eV were analyzed at a mass resolution ($m/\Delta m$) of ~4,500. The combined secondary magnet settling and dwell times per mass cycle were ca. 45 s, and 100 cycles were acquired per individual profile. These conditions resulted in-depth intervals of ~0.2 µm per cycle, with a total depth for an individual profile of ca. 20 µm. Trace element compositions were calibrated against zircon standard 91500 (Table 2 in Liu et al. 2010) analyzed under the same conditions. Intensities were normalized to $^{91}Zr^{++}$, and for calculation of concentrations, stoichiometric compositions were assumed for zircon standards and unknowns. The resulting relative sensitivity factors (RSF; measured ratio/true ratio in standard) varied systematically with depth, by nearly a factor of 2. Because of the RSF being depth-dependent, concentrations of the unknowns were corrected using a depth-matched RSF. From the reproducibility of 91500 zircon depth profiles ($n = 5$), we estimate relative uncertainties of ~10 % (Ti), ~8 % (Y and Hf), ~15 % (Ce), ~3 % (Th), and ~4 % (U). All trace element analyses reported here have uncertainties that propagate counting errors for the individual cycles and RSF errors.

Under ideal circumstances, trace element- and age-depth profiles would penetrate the same zircon domains, but we note deviations from this ideal behavior. Moreover, even if the age profile geometry was nearly equivalent to that of the trace element profile, it would be impractical to calculate (^{230}Th)/(^{238}U) ages for individual cycles in the age profiles due to the large counting uncertainties for the low intensity $^{230}ThO^{+}$ peak. Consequently, we present our trace element data in two different ways: (1) cycle-by-cycle, which permits monitoring trace element variations at high spatial resolution (ca. 0.2 µm per cycle) at relative time scales (rims being younger than interiors), and (2) binned to depth intervals of ~2–6 µm which are set by the (^{230}Th)/(^{238}U) age bins and which permit co-registering trace element variations with absolute time.

Compositional maps of Ti and Y concentrations were subsequently generated by ion imaging two of the 17 crystals which had been previously analyzed for crystallization age and trace element composition by depth profiling. Secondary ion maps were produced on the same sectioned surface as the interior age analysis described in Storm et al. (2011; 2012) and opposite the crystal face from which age and trace element profiles were drilled into the crystal (Fig. 2). They were positioned in areas of the section that show transitions in CL brightness to investigate parts of the crystal that have grown under changing chemical and potentially thermal conditions. We conducted analyses following the protocol described by Harrison and Schmitt (2007) using a Cs^{+} primary beam focused to a ~2 µm spot and measuring negatively charged Ti and Y secondary ions (e.g., TiO^{-}, YO^{-}). The smaller Cs^{+} beam diameter permits a better spatial resolution than that achievable with a $^{16}O^{-}$ beam. A further advantage is that the negative secondary ion spectrum is practically free of isobaric interferences from doubly charged ions (such as $^{96}Zr^{++}$ interfering with $^{48}Ti^{+}$ for positive secondary ions) resulting in enhanced sensitivity because of the lower mass resolution required (Harrison and Schmitt 2007). Analyses started with pre-sputtering the sample with a ~500 pA primary beam for 3 min to remove the gold coating before rastering over an area of 25 × 25 µm with ~50 pA beam. Secondary ions of $^{30}SiO_2^{-}$, $^{48}TiO^{-}$, and $^{89}YO^{-}$ were collected at 256 × 256 pixel resolution using electron multipliers in multi-collection mode over a total integration time between 4 and 6 h. We processed images using the software ENVI©. The Ti and Y counts were normalized to Si counts after averaging 8 × 8 pixels (pixel size 0.8 µm) to reduce the number of zero or undefined pixel values. Finally, we applied a color scale to rationed pixels to better visualize Ti and Y distributions.

The spatial resolution in-depth profiling is estimated from several profiles which show sharp concentration spikes (e.g., in Ti abundance for KaT2z3 at ~6 and ~12.5 µm; Fig. 3). These spikes might be caused by different processes: the positive Ti excursion at 6 µm

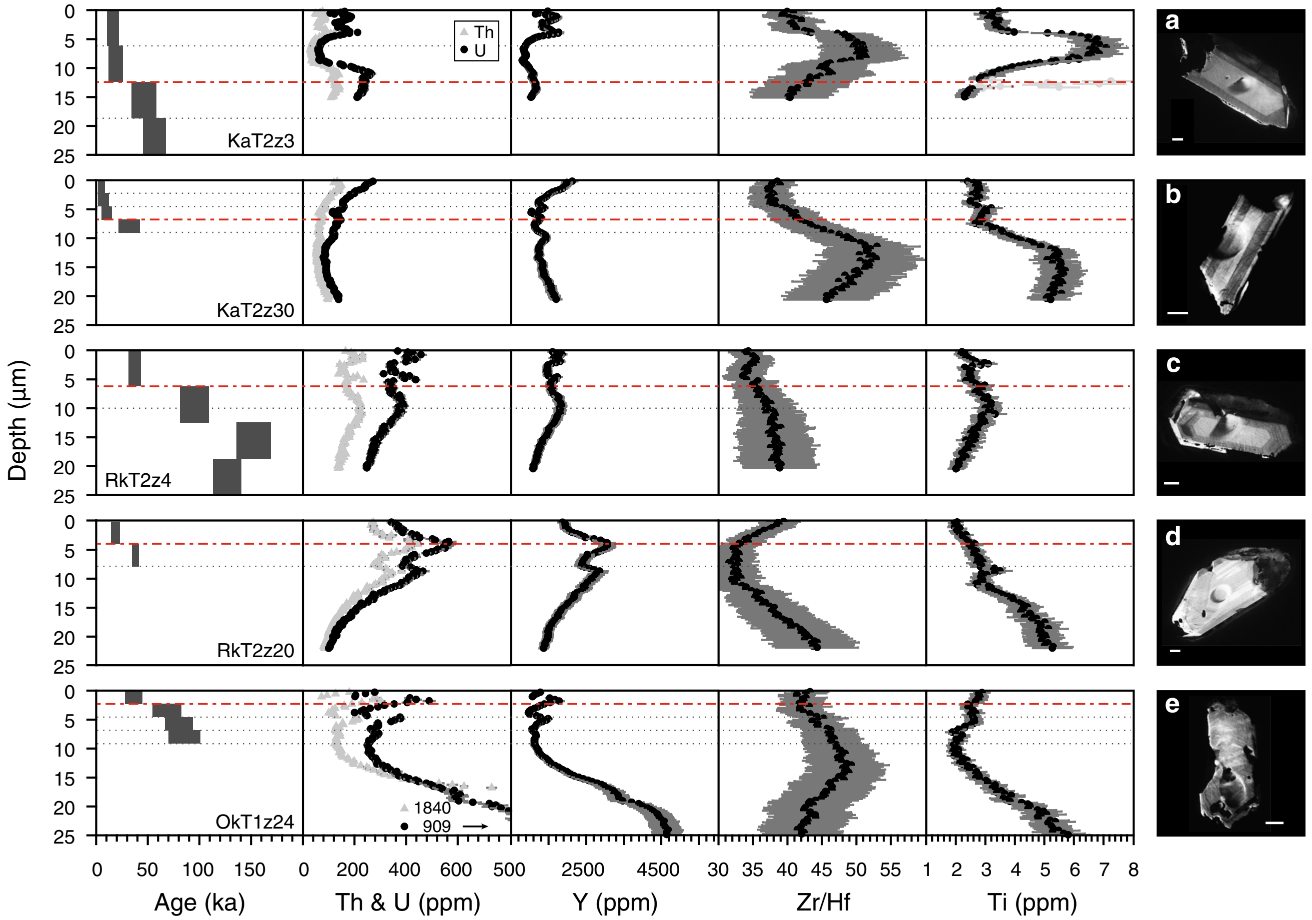

Fig. 3 Continuous compositional and age-depth profiles for selected zircons from **a** Kaharoa (Ka), **b** Waiohau (Wh), **c** Rerewhakaaitu (Rk), and **d** Okareka (Ok) eruption deposits. *Gray boxes* in the age-depth profiles represent ~30 integrated analysis cycles (~0.1 μm/cycle), with U–Th model ages at 1σ uncertainties (data from Storm et al. 2012). For compositional depth profiles, every analysis cycle is shown. *Error bars* represent 1σ uncertainties (where *no error bar* is visible, it is smaller than *symbol size*). *Light gray shaded data points* have been identified as inclusions or Ti contamination based on anomalous Ti concentrations (see text). *Gray dotted lines* mark the borders of binned age domains. *Red dashed lines* display the approximate location of hiatuses in crystal growth as indicated by discontinuous U–Th age profiles. *Arrows* indicate highest concentrations within the crystal that are out of range of the scale. CL images are for zircon interiors after sectioning crystals to ~20 μm depth. Oval pits were excavated by the ion beam during interior age spot analyses in our previous study. *White scale bars* are 20 μm long. Note that some crystals show prism faces (e.g., RkT2z4; RkT2z20) that are oblique to the sectioned faces. Profiles for all 17 grains are plotted in the Electronic Supplement. Anomalously high Ti in zircon is assigned to contamination by inclusions if Ti-in-zircon temperatures (T_{Tiz}) significantly exceed zircon saturation temperatures (T_{Zrc})

correlates with an increase in Zr/Hf and therefore likely represents a chemically distinct zircon domain, whereas the ~12.5 μm Ti spike lacks a correlation with Zr/Hf and therefore is tentatively attributed to penetration of an inclusion in zircon (Fig. 3). Regardless of the cause the rapid decay to low abundances following the spike would not be observed if a significant contribution from the shallower parts of the profile lingered on (Fig. 3). Broadening of sharp steps in crystal compositions is possible if domain boundaries were intersected at an oblique angle, for example as a result of interior crystal domain boundaries not being aligned perfectly perpendicular to the direction of sputtering. The presence of well-defined oscillatory excursions in many profiles that match in dimensions those visible in CL images (e.g., RkT2z4; Fig. 3) suggests that our mounting and analysis technique permits parallel growth layers in zircon to be resolved at a depth resolution of <1 μm. Mineral or melt inclusions are another source of artifacts, but based on the strong enrichment of Zr, Y, Ce, Hf, Th, and U in zircon relative to glass they are only considered problematic for Ti which is highly enriched in these inclusions relative to zircon. For ion imaging, the spatial resolution was determined by imaging a Ta–Si grid to ~2 μm.

Results

Zircon trace element variations and correlations

For the 17 crystals with depth profiling analyses, we obtained 1,390 individual data points at 0.2 µm intervals which record variations in zircon composition at a spatial scale that is two orders of magnitude better than commonly achieved in SIMS spot analyses and commensurate to that of electron beam CL imaging (Fig. 3; Electronic Supplementary Material). Before investigating the in-depth variability of the profiles and the relationships between trace elements and U–Th ages, we first evaluate the overall data set to outline the significance of individual zircon trace element parameters (abundances and ratios) as indicators of melt composition and temperature. Scatter plots of such large data sets often obscure the bulk of the data, and attention is diverted to outliers. Thus, we plot the data as 2D probability density contours to better document the actual data distribution. Two-dimensional probability density diagrams for Ce, Y, Th, and U against Zr/Hf (Fig. 4) show skewed fields indicating negative correlations. To constrain correlation coefficients (r) between the plotting parameters and at the same time removing bias toward outliers, we ranked the x-axis values from lowest to highest and binned them at intervals of 100 analyses. Median values were then calculated for each bin, and linear correlations were fitted to the binned data (Fig. 4). Significant correlations were found with $r = -0.89$ (Ce), -0.85 (Y), -0.92 (Th), and -0.97 (U), whereas Th/U lacks strong systematic variations with Zr/Hf ($r = -0.43$) (Fig. 4). The correlations of Th and U with Ti are strong ($r = -0.73$ and -0.91, respectively), whereas those of Ce (0.14), Th/U (0.46), and Y (-0.02) with Ti are low. Y is a special case in that it is positively correlated with U, albeit with two sub-parallel trends (Fig. 5a). The presence of two types of zircon (high and low Y/U) broadens the 2-D probability density fields in the Y versus Zr/Hf or Ti plots (Fig. 4).

Zircon thermometry constraints

Guided by the strong correlation between Zr/Hf and Ti ($r = 0.86$), which supports the notion that both are temperature controlled (Fig. 5b), we quantified the temperature range over which zircon crystallized using the calibrations of Watson and Harrison (1983) and Boehnke et al. (2013) for zircon saturation temperatures (T_{Zrc}) and Ferry and Watson (2007) for Ti-in-zircon temperatures (T_{Tiz}). Zircon saturation temperatures are based on OVC whole-rock compositions (Electronic Supplementary Material), a reasonable assumption for the comparatively low crystallinity of the rocks (whole-rock compositions from Speed et al. 2002; Nairn et al. 2004; Shane et al. 2007, 2008a). Depending on the calibration, these temperatures range between ~740 and 810 °C (Watson and Harrison 1983) and ~690 and 770 °C (Boehnke et al. 2013). We model T_{Tiz} under the assumption that the ubiquity of quartz in Tarawera rocks constrains $a_{\mathrm{SiO_2}} = 1$. We then estimate temperatures as a function of variable $a_{\mathrm{TiO_2}}$, for which we narrow plausible ranges using coexisting Fe–Ti oxides. The T_{Tiz} isolines are then plotted as T versus $a_{\mathrm{TiO_2}}$ along with Tarawera Fe–Ti oxide derived temperatures and $a_{\mathrm{TiO_2}}$ (from Speed et al. 2002; Nairn et al. 2004; Shane et al. 2007, 2008a; Shane unpublished data) in Fig. 6, following the approach of Ghiorso and Gualda (2012). The range of $a_{\mathrm{TiO_2}}$ defined by Tarawera Fe–Ti oxides (touching crystal pairs which also meet the Mg/Mn exchange criterion of Bacon and Hirschmann 1988) then constrains a model temperature range for zircon crystallization (Fig. 6). We have no direct constraints on $a_{\mathrm{TiO_2}}$ at the time of crystallization of individual zircon domains, but useful limits can be derived by combining low-T $a_{\mathrm{TiO_2}}$ of ~0.5 with high Ti in zircon (~12 ppm) and high-T $a_{\mathrm{TiO_2}}$ of ~0.7 with low Ti in zircon (~2 ppm), based on the assumption that equilibrium melt $a_{\mathrm{TiO_2}}$ is negatively correlated with T (Ghiorso and Gualda 2012). This yields an apparent temperature difference between the highest and lowest Ti zircons of ~200 °C. Inversion (low $a_{\mathrm{TiO_2}}$ for high-Ti zircons and high $a_{\mathrm{TiO_2}}$ for low-Ti zircons) would cause the apparent temperature difference to decrease to ~130 °C. The T_{Tiz} temperature range broadly agrees with the ~100 °C temperature interval between the highest T_{Zrc} and the water-saturated rhyolite solidus of ~680 °C at upper crustal pressures (Holtz and Johannes 1994). Many T_{Tiz} fall below T_{Zrc} and at high $a_{\mathrm{TiO_2}}$ would yield subsolidus T_{Tiz} ~650 °C. Similarly, low model T_{Tiz} has been reported for rhyolites elsewhere (including the Bishop Tuff; Reid et al. 2011), and it remains unclear whether these low temperature estimates reflect subsolidus zircon crystallization or whether they are an artifact of the thermometer's calibration. The positive trend in $a_{\mathrm{TiO_2}}$ versus T for Tarawera Fe–Ti oxides (Fig. 6) is nearly identical to that reported for Bishop Tuff, which Ghiorso and Gualda (2012) interpreted to result from Fe–Ti oxide disequilibrium. For Tarawera deposits, this interpretation is unsatisfactory because Fe–Ti oxide compositions for individual Tarawera eruptions fall into tightly clustered $a_{\mathrm{TiO_2}}$ versus T fields (Fig. 6). We acknowledge that systematic uncertainties of model T_{Tiz} impede comparison with other thermometers, but maintain that the first-order systematic relations between temperature-sensitive parameters Ti and Zr/Hf in zircon reflect changing magmatic temperatures on the order of ~130–200 °C. This is corroborated by the systematic relationships between

Fig. 4 Co-variations between Zr/Hf as a measure of zircon fractionation and trace elements (**a**–**e**) and Ti as an indicator for temperature changes and trace elements (**f**–**j**). Two-dimensional probability density contour plots are generated from individual cycles (n = 1,390) of the depth profiles. The *colored zones* are based on relative data density probability and indicate decreasing relative probability from *red* to *blue*. *Red lines* are based on linear regression of binned data, and the correlation coefficient (r) indicates goodness of fit of that line

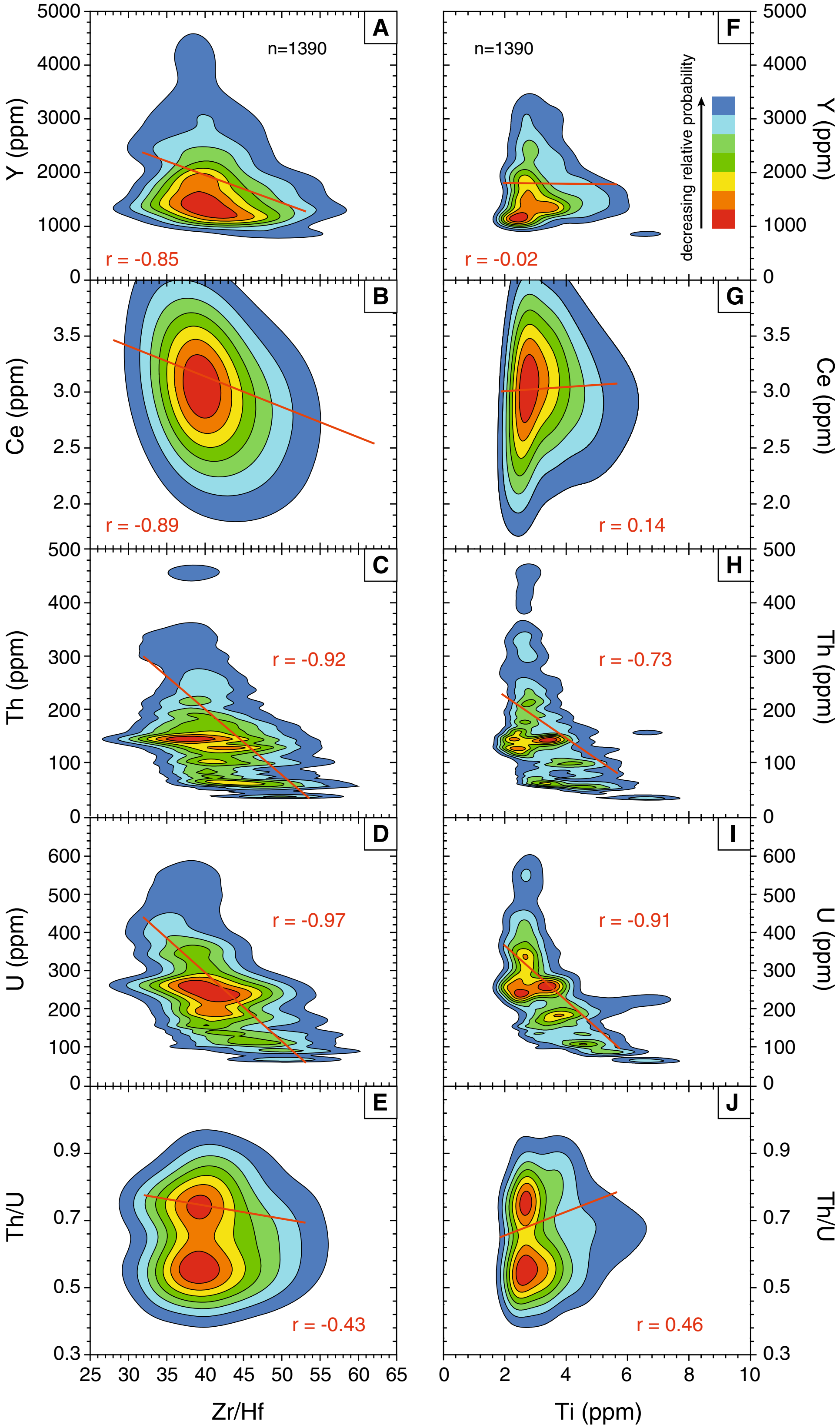

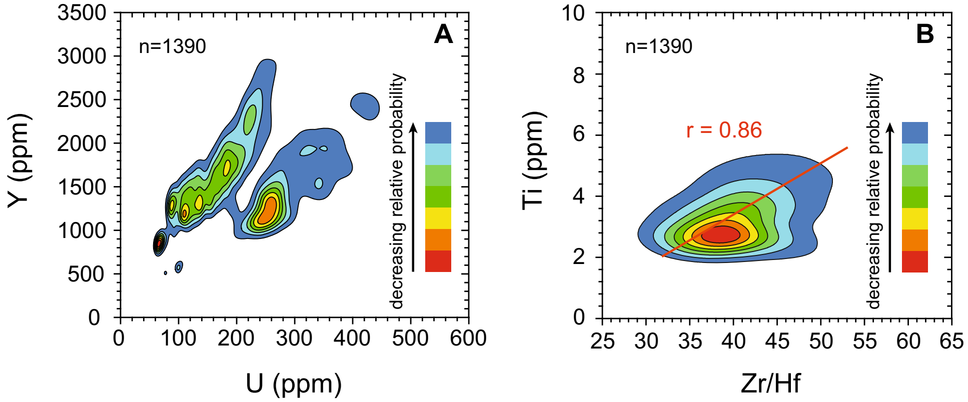

Fig. 5 Co-variations between **a** Y and U concentration and **b** Ti and Zr/Hf. Two-dimensional probability density contour plots are generated from individual cycles ($n = 1{,}390$) from the depth profiles. The colored zones are based on relative data density probability and indicate decreasing relative probability from *red* to *blue*. The *red line* is based on linear regression, and the correlation coefficient (r) indicates goodness of fit of that *line*

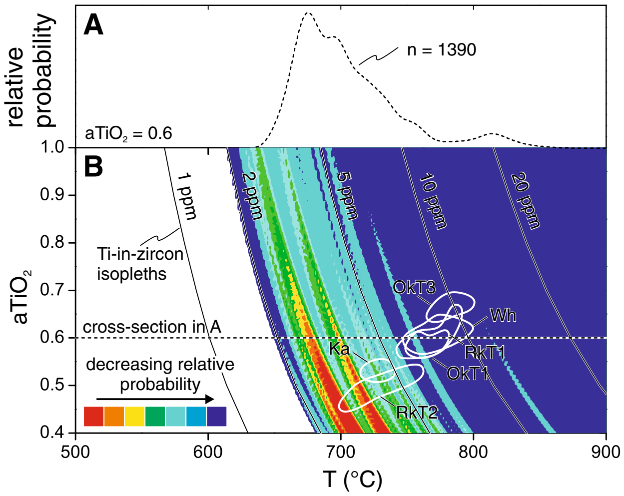

Fig. 6 Probability density for Ti-in-zircon thermometry using measured Ti abundances from zircon depth profile intervals ($n = 1{,}390$) to calculate temperature T_{Tiz} as a function of Ti activity $a_{\mathrm{TiO_2}}$. **a** One-dimensional probability distribution for fixed $a_{\mathrm{TiO_2}} = 0.6$ (cross-section line in **b**). **b** Two-dimensional probability distribution of T_{Tiz} with variable $a_{\mathrm{TiO_2}}$. Isopleths were calculated using the calibration from Ferry and Watson (2007) assuming melt $a_{\mathrm{SiO_2}} = 1$. Individual analyses and uncertainties are color coded according to their probability. Fields outlined in *white* show $a_{\mathrm{TiO_2}}$ and temperature T (in °C) calculated for coexisting Fe–Ti oxides in Tarawera rhyolites (Ka = Kahaora; Wh = Waiohau; RkT1 and RkT2 = Rerewhakaaitu; OkT1 and OkT3 = Okareka) using the calibration of Ghiorso and Gualda (2012). Note that fields for individual eruptions are narrow, suggesting that $a_{\mathrm{TiO_2}}$ estimates should not be significantly impacted by Fe–Ti oxide disequilibrium generated by rapid crystallization at the time of eruption. The cross-section at an intermediate $a_{\mathrm{TiO_2}} = 0.6$ defined by Fe–Ti oxides illustrates the characteristic T_{Tiz} temperature distribution for Tarawera zircons with a dominant low-T peak (T_{Tiz} ~680 °C) and high values defining a minor peak at ~810 °C. Regardless of uncertainties of $a_{\mathrm{TiO_2}}$ at the time of zircon crystallization, the observed Ti variations in zircon require crystallization over an ~130–200 °C temperature interval (see text)

incompatible trace elements in zircon (e.g., Y, Th, U) and decreasing Ti and Zr/Hf (Fig. 4), which are indicative of crystallization during cooling (retrograde zircon crystallization).

Zircon trace element variations on relative crystallization timescales

Within individual zircon crystals, trace element compositions (Th, U, Y, Ti, Ce, and Zr/Hf) can vary by factors of up to four (Fig. 3). Ti abundances in rim domains are almost always low or at least at the same level, when compared to crystal interiors (Fig. 3). This is also reflected in the prevailing rimward decrease in Ti which is the case for ~50 % of the total profiled depth in zircons studied here. Depth intervals with invariant Ti (~30 %) and rimward increases in Ti (~20 %) are less common. Another shared feature in many profiles is minor oscillatory zonation in Y, Th, and U which are commonly highly correlated (e.g., RkT2z20, OkT3z12; Fig. 3). However, oscillatory zonation is not reflected in Zr/Hf or Ti, which vary monotonically in the profiled crystals.

Despite these general commonalities, we note a striking absence of any prevailing trends, and often the presence of reversals, in individual trace element depth profiles for Tarawera zircon crystals. Incompatible elements such as Y, Th, and U show rimward enrichment (e.g., KaT1z35, KaT2z30, RkT2z20; Fig. 3; Electronic Supplementary Material) or depletion (e.g., Whz5, OkT1z24; Fig. 3; Electronic Supplementary Material). Similarly, temperature indicators such as Zr/Hf and Ti show rimward decreases (e.g., KaT1z35 and KaT2z3 between ~0 and 10 µm; Fig. 3), increases (the same crystals between ~10 and

20 μm), or inverse correlations (e.g., OkT1z24; Fig. 3). In a few cases, the correlation changes within the same crystal (e.g., RkT2z4, RkT2z20; Fig. 3). High-Ti domains (barring those assigned to contamination by inclusions) often have low Y, Th, and U (e.g., KaT2z30 ~15–20 μm; RkT2z20 ~15–20 μm; Fig. 3) which would be expected for zircon crystallization in a less evolved hotter melt, and hence lower incompatible trace element abundances. Prominent exceptions to this behavior exist whereby some of the highest Y, Th, and U abundances are associated with high Ti (e.g., in KaT1z18 or OkT1z24; Fig. 3).

Individual depth profiles from crystals in the same sample that temporally overlap also record contrasting behavior. For example, zircon KaT2z30 (Fig. 3) has a rim age that is essentially indistinguishable from the eruption age indicating crystallization until just prior to eruption. Within the profile for KaT2z30, Ti abundance monotonically decreases rimward, whereas Y, Th, and U abundances increase. Zr/Hf variations parallel those of Ti, supporting the notion that a rimward Ti decrease reflects declining temperature. Zircon KaT1z18 (Electronic Supplementary Material) from the same eruption and with a comparable rim age also shows a rimward decrease in Ti. However, in this case, the trend is positively correlated with Y, Th, U, and Th/U, whereas Zr/Hf conversely increases toward the rim. A third crystal from the Kaharoa eruption (KaT2z3, Fig. 3) collected from the same hand sample as KaT2z30 shows yet another behavior. Its interior is consistently low in Zr/Hf and Ti (barring a sharp Ti spike at ~12.5 μm depth which we interpret as being an inclusion in the zircon). Crystal KaT2z3 shows a prominent positive Ti and Zr/Hf excursion centered at ~6 μm depth that is of nearly the same magnitude as the overall variation displayed by crystals KaT1z18 and KaT2z30. The rim zone of crystal KaT2z3 reverts to low Ti and Zr/Hf values that are nearly identical to those of its interior.

We have evidence for sharp age breaks or hiatuses of up to ~40 ka which we previously detected in eight of the depth-profiled zircons (Storm et al. 2012). These age breaks generally correspond to compositional changes such as jumps to either higher (e.g., U, Th, Y, and Th/U in RkT2z4) or lower (e.g., U, Th, and Y in OkT3z18) concentration (Fig. 3; Electronic Supplementary Material). Some hiatuses are associated with a reversal in the zonation pattern (e.g., Zr/Hf and Ce in RkT2z4; U, Th, Y, Ce, and Zr/Hf in RkT2z20; Fig. 3). However, not all of the elements display changes coinciding with these hiatuses (e.g., Ti in RkT2z4 and RkT2z20; Zr/Hf, Ce, and Ti in RkT2z23; Fig. 3; Electronic Supplementary Material). Although the changes in chemistry at these hiatuses differ from crystal to crystal, we find that a rimward decrease in U after the break is often accompanied by higher Ti compared to the abundances before the break (KaT2z3, Fig. 4a; OkT3z12 and OkT1z24; Fig. 3; Electronic Supplementary Material). This is consistent with intermittent zircon resorption, followed by overgrowth from a hotter and less evolved melt. Potential resorption features are also evident as embayments (RkT2z5) or inclusions (OkT3z12) in some CL images (Fig. 3; Electronic Supplementary Material).

Trace element ion imaging in correlation with CL activity

In order to explore the relationship between elemental variation and CL intensities, we evaluated the 2D distribution of Y (an incompatible trace element) and Ti (a temperature-sensitive indicator) in zircon via high-sensitivity secondary ion distribution mapping (Fig. 7). The main goal of this was to test whether Ti partitioning could be affected by elevated trace element abundances (represented by the xenotime substitution involving Y) and thus may not reflect temperature (Hofmann et al. 2009). In zircon KaT2z3, the Y distribution pattern corresponds to the CL pattern, with high concentrations in dark CL zones and a relatively sharp transition from low to medium and high-Y concentrations coinciding with the sharp CL boundary between light core and dark rim (Fig. 7a). Zircon RkT2z4 also shows a broad match in the shapes of Y and CL zonation with high-Y domains generally being CL dark, but the contrast in CL shading clearly does not directly correlate with variations in Y abundance (compare similar CL gray in images '5' and '6' with different levels of Y; Fig. 7c). In contrast to Y concentrations, the distribution of Ti concentrations is heterogeneous in domains parallel to the crystal face and cuts across the CL pattern, with high-Ti concentrations in both dark and light CL zones (KaT2z3; Fig. 7b). Maps '3' and '4' in KaT2z3 show local high-Ti domains at the μm-scale. These cause Ti ion intensities to vary over the analyzed area with variations that cross-cut CL zonation. We interpret these variations as artifacts from Ti-bearing surface contamination, similar to those detected by Hofmann et al. (2009) using Nano-SIMS to image Ti-distribution in zircon. Note that these surface effects are only apparent in secondary ion imaging at low sputter rates and not when applying much stronger primary beams in-depth profiling which rapidly removed surficial contamination. The Ti ion map in zircon RkT2z4 is free of such artifacts from surface contamination and lacks any distinct variation across the imaged areas that display distinct CL features with a high contrast in brightness (Fig. 7d).

Zircon trace element variations at absolute timescales

In most cases, correlation between the U–Th age and trace element profiles was achieved at high confidence using U

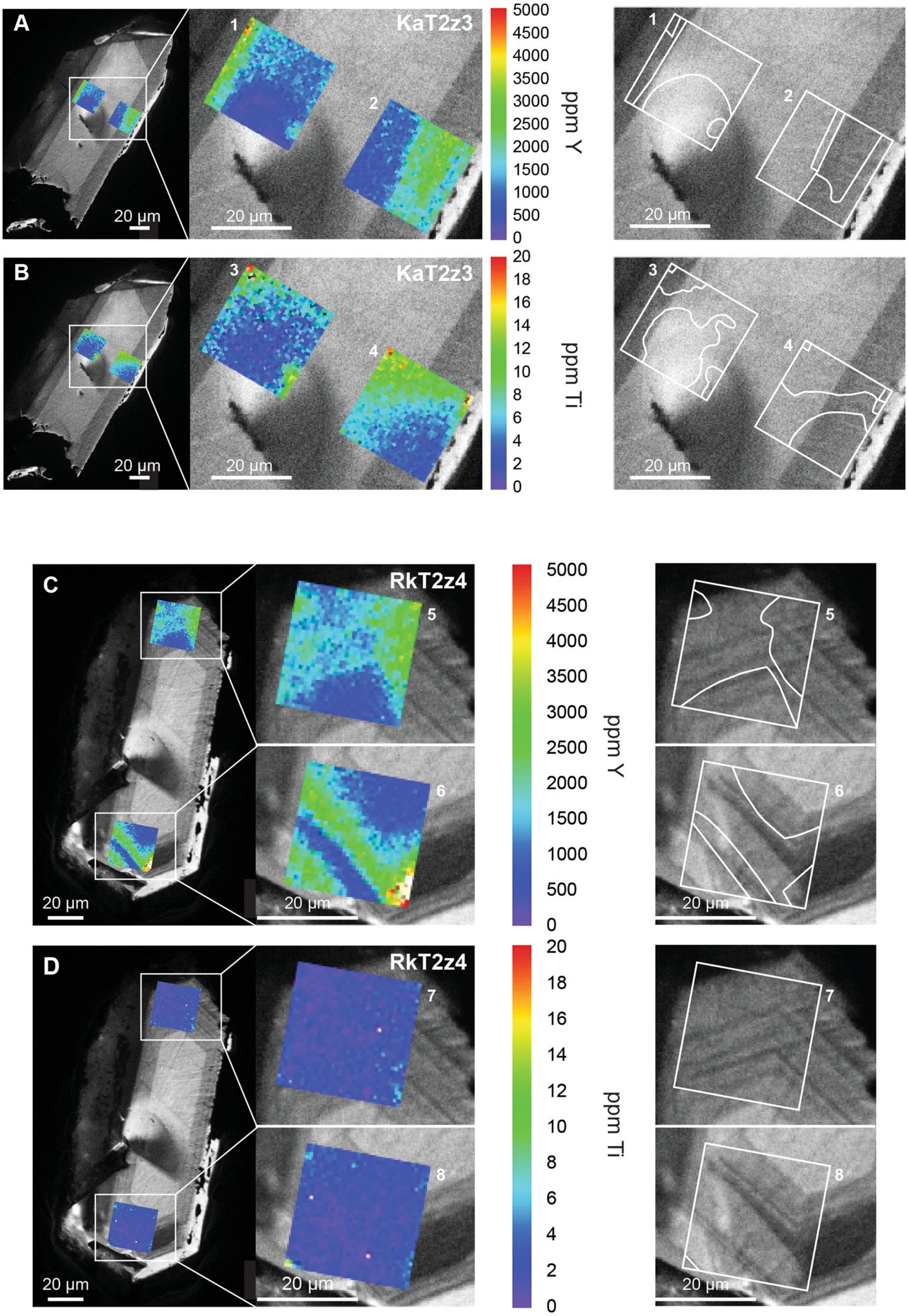

Fig. 7 Ion images for elemental concentrations overlain on CL images of the crystals. *Panels on right* illustrate the aerial boundaries between distinct Y and Ti concentration domains to facilitate the comparison with CL brightness variations

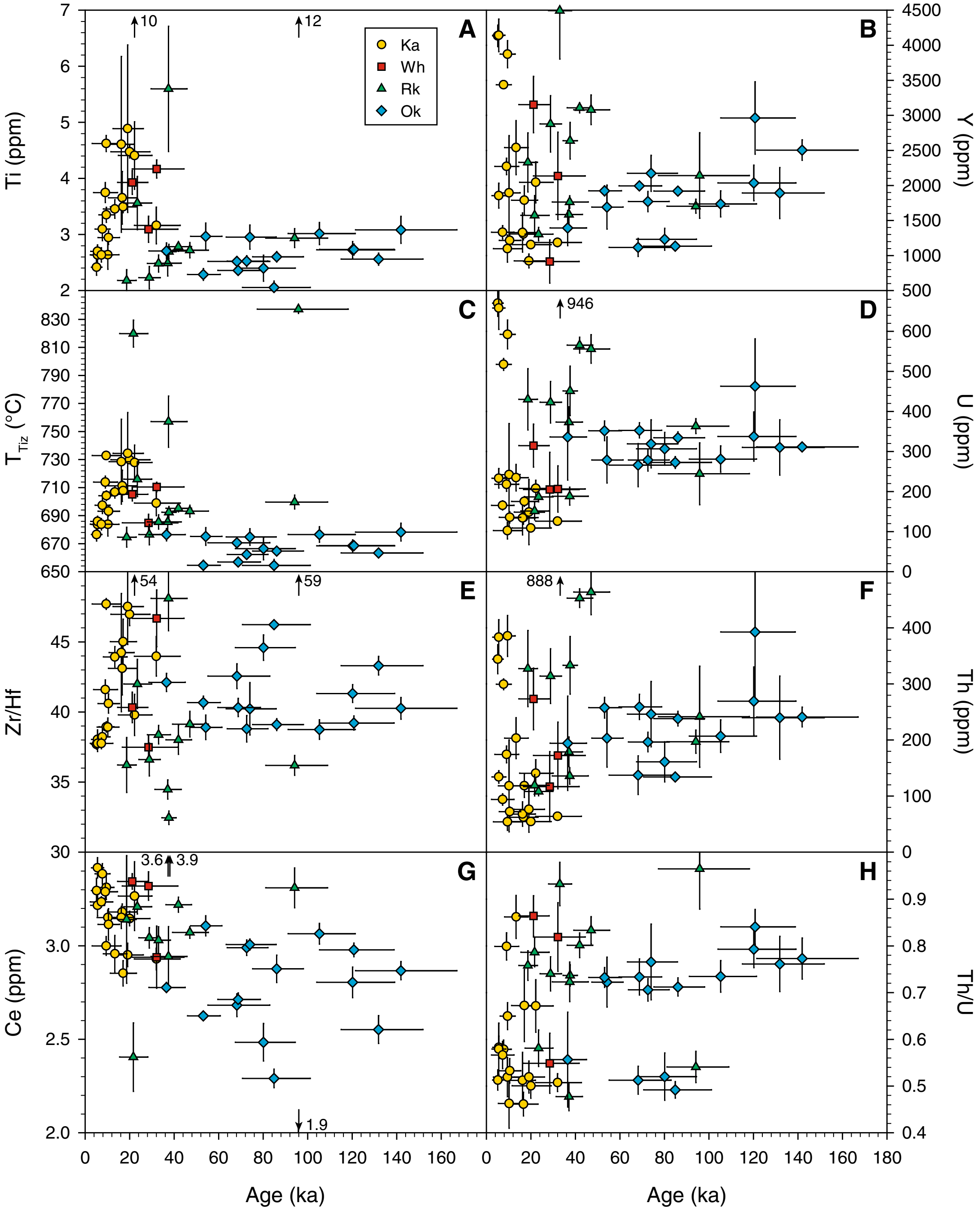

Fig. 8 Composition of dated zircon sub-crystal domains plotted against age; model T_{Tiz} are calculated for $a_{\mathrm{TiO_2}} = 0.6$ with *error bars* reflecting only analytical uncertainties, not uncertainties in $a_{\mathrm{TiO_2}}$ (see text). The compositional depth profiling data have been binned corresponding to the respective age bins (see text). *Error bars* represent 1σ uncertainties. *Ka* Kaharoa, *Wh* Waiohau, *Rw* Rerewhakaaitu, *Ok* Okareka

and Th abundances (Fig. 3; Electronic Supplementary Material). Because we have previously binned U–Th age data at regular depth intervals (2–6 μm depending on primary beam intensity), trace element data were averaged over the same intervals. This procedure limits the depth resolution for the trace element analysis, but yields age-composition data pairs that are comparable to conventional ion microprobe spot analyses, albeit at a ~10-times better spatial resolution. Some age and trace element profiles could not be correlated by the U and Th concentration

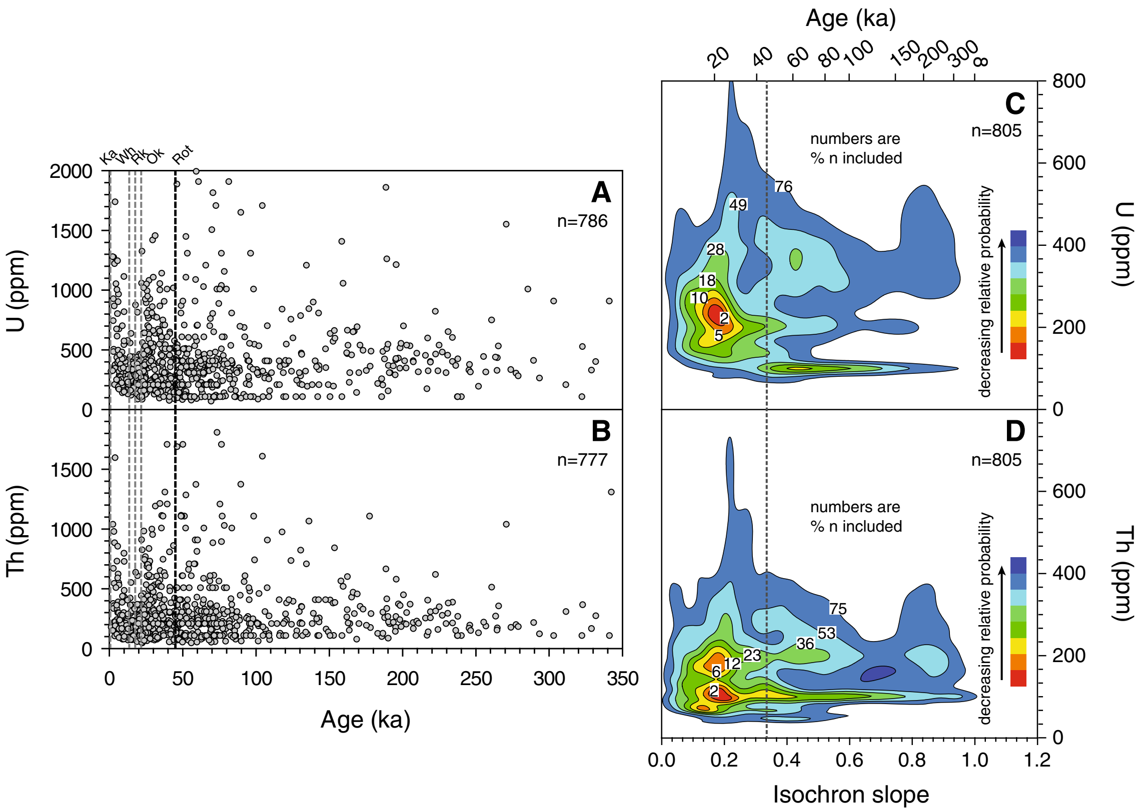

Fig. 9 U and Th composition versus age for 805 analyses of zircons from the OVC including Tarawera rhyolites (Storm et al. 2012) and granitoids (Shane et al. 2012), Rotoiti rhyolites (Charlier and Wilson 2010; Danišík et al. 2012), Earthquake Flat rhyolite (Danišík et al. 2012), and Mangaone subgroup rhyolites (Charlier and Wilson 2010). **a**, **b** *Scatter plots* showing individual analyses. Outliers are omitted for clarity. *Dashed lines* mark the age of the Tarawera eruptions (Ka, Wh, Rk, Ok) and the Rotoiti eruption (Rot). **c**, **d** Two-dimensional probability density *contour plots* generated from the same data as the *scatter plots*. Note that the scale is different from *scatter plots*. Data not visible in the *contour plots* reflect low density of points. The *colored zones* are based on relative data density probability and indicate decreasing relative probability from *red* to *light blue*. The *numbers* represent the percentage of analysis cycles included in the *contour*

signals. The lack of correlation in zonation revealed in adjacent profiles indicates that some crystals have complex geometries such as asymmetrical growth or irregular zonation (Electronic Supplementary Material). These profiles are not examined in any detail here.

The 15 zircon crystals where U and Th variations permitted correlation between trace element- and age-depth profiles yield 48 individual crystal domains ranging in age between ~5 and ~142 ka (Fig. 8). A striking feature in this data set is that the younger zircon domains (<45 ka) typically show a wider range in trace element abundances compared to older zircon domains. The young population is dominated by Ka and Wh samples, whereas the older population comprises mostly Rk and Ok zircon crystals, despite the fact that their eruption ages are all <45 ka. With few exceptions, a pattern emerges where Ti and Ce concentrations and Zr/Hf are generally the highest in <45 ka zircon domains (Fig. 8). Y, Th, and U abundances are often more extreme (showing both lower and higher values) in <45 zircon domains, and many of these zircon domains also show comparatively low Th/U (Fig. 8).

To test whether these temporal patterns are an artifact of our small depth profiling sample subset, more than 800 published zircon ages from OVC rhyolites that report Th and U abundances were examined (Fig. 9). In addition to Tarawera deposits, these data include crystals from Rotoiti, Earthquake Flat, and the Mangaone subgroup deposits (Charlier and Wilson 2010; Storm et al. 2012; Shane et al. 2012; Danišík et al. 2012). Although high U and Th crystals occur throughout an ~350 ka age span, there is more spread and an overall higher average in the <45 ka population as illustrated by the 2D probability density contouring (Fig. 9). This suggests that a change in the diversity of zircon compositions at ~45 ka is not a sampling artifact.

Discussion

Implications for magmatic processes

The thermal and physical state of upper crustal (<10 km depth) rhyolite magma accumulation remains debated, with opposing views of long-lived mush zones with significant melt fractions (e.g., Bachmann and Bergantz 2004; Gelman et al. 2013) versus individually short-lived intrusive pulses that rapidly undergo subsolidus re-equilibration and cumulatively aggregate into batholithic bodies (e.g., Glazner et al. 2004; Tappa et al. 2011; Zimmerer and Mcintosh 2012). It is therefore essential to distinguish between a synchronized thermochemical evolution and divergent crystallization paths recorded in crystals from individual magma systems. Several lines of evidence underscore that variations in secondary ion intensities recorded in-depth profiles of Tarawera zircon crystals accurately reflect compositional zonation in zircon: (1) trace element indicators generally show systematic behavior (e.g., positive correlations between Ti and Zr/Hf; negative correlations between incompatible trace elements such as U, Th, Y, and Ce with Zr/Hf); (2) trace element excursions (at ~1 μm depth intervals; Fig. 3) are sharply resolved and lack the broadening that would result from edge contributions during sputtering; and (3) there is little (<10 %) in-depth variation with relative sensitivity factors relative to the overall range of trace element variations, and these are monitored and corrected for through depth profiling of standards under the same analytical conditions. The anomalous high-Ti excursions seen in some profiles (e.g., Fig. 3) are ascribed to the presence of melt inclusions. We cautiously exclude these data from consideration unless other chemical indicators support high Ti abundances in zircon, such as covariance with Zr/Hf. A drawback of our analytical approach is that long analysis durations limit the number of profiles that can be reasonably investigated. Thus, we cannot confidently characterize chemical features that may distinguish the different magma types that fed the Tarawera eruptions (Speed et al. 2002; Nairn et al. 2004; Shane et al. 2007, 2008a). Despite this limitation, even a small number of zircons can unambiguously demonstrate that heterogeneous conditions prevailed in different parts of the magma system and that these different parts at various times contributed crystals to the erupted magmas.

Zircon depth profiling reveals both relative and absolute chronologies of the thermal and compositional conditions of the melt because diffusion of highly charged cations in zircon is vanishingly slow at magmatic temperatures, as indicated by the preservation of delicate CL banding (e.g., Cherniak et al. 1997). Retrograde zircon crystallization is triggered by a decrease in melt temperature whereby the Zr saturation concentration decreases with decreasing temperature (e.g., Watson and Harrison 1983; Harrison et al. 2007; Boehnke et al. 2013). Isothermal or prograde (upon temperature increase) zircon crystallization scenarios are conceivable, but they would require changes in melt composition and Zr abundance to counteract the zircon-destabilizing effect of increasing temperature. For example, intrusion of a Zr-rich magma could promote zircon growth if the Zr increase outweighs the increase in temperature and M (see above; Watson and Harrison 1983; Boehnke et al. 2013) expected in a less evolved magma. Resorption of small zircon crystals with unfavorable surface to volume ratios could also increase Zr abundance in the melt under isothermal or prograde conditions. This, and the likelihood of larger crystals surviving intermittent heating, conceivably produces high-T zircon overgrowths on low-T nuclei. There is evidence for intermittent heating periods in Tarawera magmas that were short-lived as indicated by steep diffusion gradients of Ti in quartz representing durations of ~100–1,000 years at temperatures >800 °C (Shane et al. 2008b). This could have resulted in partial resorption of zircon. Another scenario for zircon formation is a drop in H_2O activity which triggers crystallization of major mineral phases. This will result in an increase of Zr in the melt. An influx of hot CO_2-rich fluid or release of latent heat of crystallization could cause such an intermittent positive thermal excursion (Reid et al. 2011).

The prevalence of a rimward decrease of Ti in Tarawera zircons (Fig. 3) is consistent with crystallization controlled by oversaturation upon cooling. This is also consistent with a systematic decrease in Zr/Hf (with Zr being more compatible than Hf in zircon; Linnen and Keppler 2002) and increase in Y, Th, and U. Enhanced Ti partitioning in impure zircon has previously been asserted (e.g., Hofmann et al. 2009; cf. Reid et al. 2011), but this is unsupported by the homogeneity in Ti over domains with highly variable Y (Fig. 7). Although Y, Th, and U are compatible in zircon (e.g., Blundy and Wood 2003), the low abundance of zircon in the fractionating assemblage causes bulk-D values for these elements to be <1. The mostly negative correlation of Ce with Zr/Hf suggests that Ce is also controlled by zircon fractionation (e.g.,Claiborne et al. 2010a), possibly compounded by the effects of variable oxygen fugacity on Ce (Trail et al. 2011).

In a few Tarawera zircons, prograde crystallization episodes are superimposed on the retrograde crystallization trend (e.g., KaT2z3 and KaT1z35, Fig. 3; Electronic Supplementary Material). Although heating is expected to counteract zircon crystallization, it is conceivable that a heating episode leading to resorption (especially of small crystals) is followed by renewed zircon crystallization at higher temperatures. In some crystals (e.g., KaT1z18; OkT1z24, Fig. 3), high Y, Th, or U abundances exist in interior domains which also display high-Ti content. This may reflect zircon crystallization in an environment where incompatible elements are locally enriched, e.g., a melt pocket that experienced rapid crystallization of major phases such as Fe–Ti oxides at high temperature (Bacon 1989).

Elemental ratios of isovalent cations such as Zr/Hf are relatively insensitive to temperature changes and kinetic effects (unless they are elements affected by oxidation state, such as U and Ce) and thus provide insight into crystallization histories. Kaharoa melt (glass) has Zr/Hf ~25 (Nairn et al. 2004), which would be in equilibrium with zircon at Zr/Hf ~57 (relative partitioning values from Blundy and Wood 1994, 2003). This is indistinguishable from the upper end of the values recorded in Kaharoa zircons (~60; Fig. 3). To produce zircons at the lower end of the Zr/Hf range (~29) would require Zr-depleted melts (Zr/Hf = ~13). The abundance of zircon in the fractionating mineral assemblage (with major phases being equally incompatible for Zr and Hf) is difficult to quantify, but for maximum estimates of <0.1 % (from the zircon yield in mineral separation), the remaining melt fraction would be <30 %.

Low melt fractions indicated by zircon crystals with low Zr/Hf imply that the magma reached higher crystallinity levels at times prior to eruption than those prevailing in the erupted magma at the time of eruption. There is additional evidence for high crystallinity in parts of the magma system prior to eruption: Melt inclusions trapped in resorbed quartz in some eruption deposits are more evolved than the accompanying matrix glass, requiring higher degrees of fractionation (Shane et al. 2008b). Near solidus conditions could also explain growth hiatuses in zircon that lack resorption surfaces and display euhedral crystal faces that predate eruption by 10^3–10^4 years (Storm et al. 2012).

Regardless of the relative influences of closed-system crystallization and open-system recharge on zircon compositions, the geochemical diversity of the zircon crystals such as opposing zonation patterns in crystals extracted from the same hand specimen argues against any simple history involving large parts of the magmatic system. Storm et al. (2012) reached a similar conclusion based on disparate ages of crystal faces and rates of crystal growth. Instead, considerable pre-eruptive crystal transport and mixing from heterogeneous environments is required, and the zircons are better described as a ‘crystal cargo.’ Similar origins appear to be shared by other phases in the Tarawera rhyolites such as amphiboles (Shane and Smith 2013).

Implications for magma evolution within the Okataina Volcanic Center

Despite the considerable diversity in Tarawera zircon compositions, directly dated domains within the crystals provide an opportunity to identify temporal magmatic trends and compare them to those evident from whole-rock and major mineral geochemistry. There was a dramatic change in erupted magmas following the ~45 ka Rotoiti caldera eruption (Shane et al. 2005b; Smith et al. 2005) (Fig. 10). Intra-caldera eruptions at ~43–35 ka emitted hotter, less evolved magmas (rhyodacites), followed by progressively more evolved and cooler magmas between ~35 and 30 ka, based on whole-rock and major mineral compositions. In contrast, rhyolites erupted post-26 ka were mostly high SiO_2 and were dominated by hydrous ferromagnesian mineralogies which display petrologic evidence for lower T and P conditions for magmatic differentiation (e.g., Shane et al. 2007, 2008a).

Based on the geochemistry of zircon crystals in the youngest eruptive deposits from the Haroharo and Tarawera volcanoes, Klemetti et al. (2011) argued for an episode of magmatic recharge at 40–30 ka signaled by high-Y concentrations in zircon that broadly mirror the compositional history of erupted magma. Zircon geochemistry determined by depth profiling also reveals a significant change in compositional patterns post-45 ka (Figs. 8, 10). However, our new data do not support a pervasive compositional change in the entire magmatic system. The dated micron-scale zircon domains in the ~30–40 ka interval variably display higher or lower Y contents (and other elements) compared to preceding age domains (Fig. 10). We also observe high-Y zircon in the post-26 ka interval, when erupted magmas returned to higher-SiO_2 rhyolite (Fig. 10).

It is possible that these features went undetected in Klemetti et al.’s (2011) data because their ~25-μm-diameter ion beam imprint across sectioned crystals did not permit the youngest zircon growth domains to be distinguished. In addition, their interior ages could also represent an integration of several finely zoned age domains. These problems are compounded by their assumption that zircons grew at a constant rate up to eruption. Age-depth profiling demonstrates hiatuses which imply that growth rates were highly variable (Storm et al. 2012). Moreover, many crystals terminated growth tens of thousands of years before eruption (Storm et al. 2012). The heterogeneous compositions and crystallization temperatures seen in the post-45 ka zircon domains are more likely to develop in a system where small, isolated melt pockets evolved independently. Therefore, parallel trends in Y versus U for some zircon crystals could be related to localized fractional crystallization with different mineral parageneses. This suggests limited interconnectivity in the magmatic system, an observation supported by other petrologic data such as the co-eruption of different melts and their associated mineral assemblages (e.g., Shane et al. 2008b).

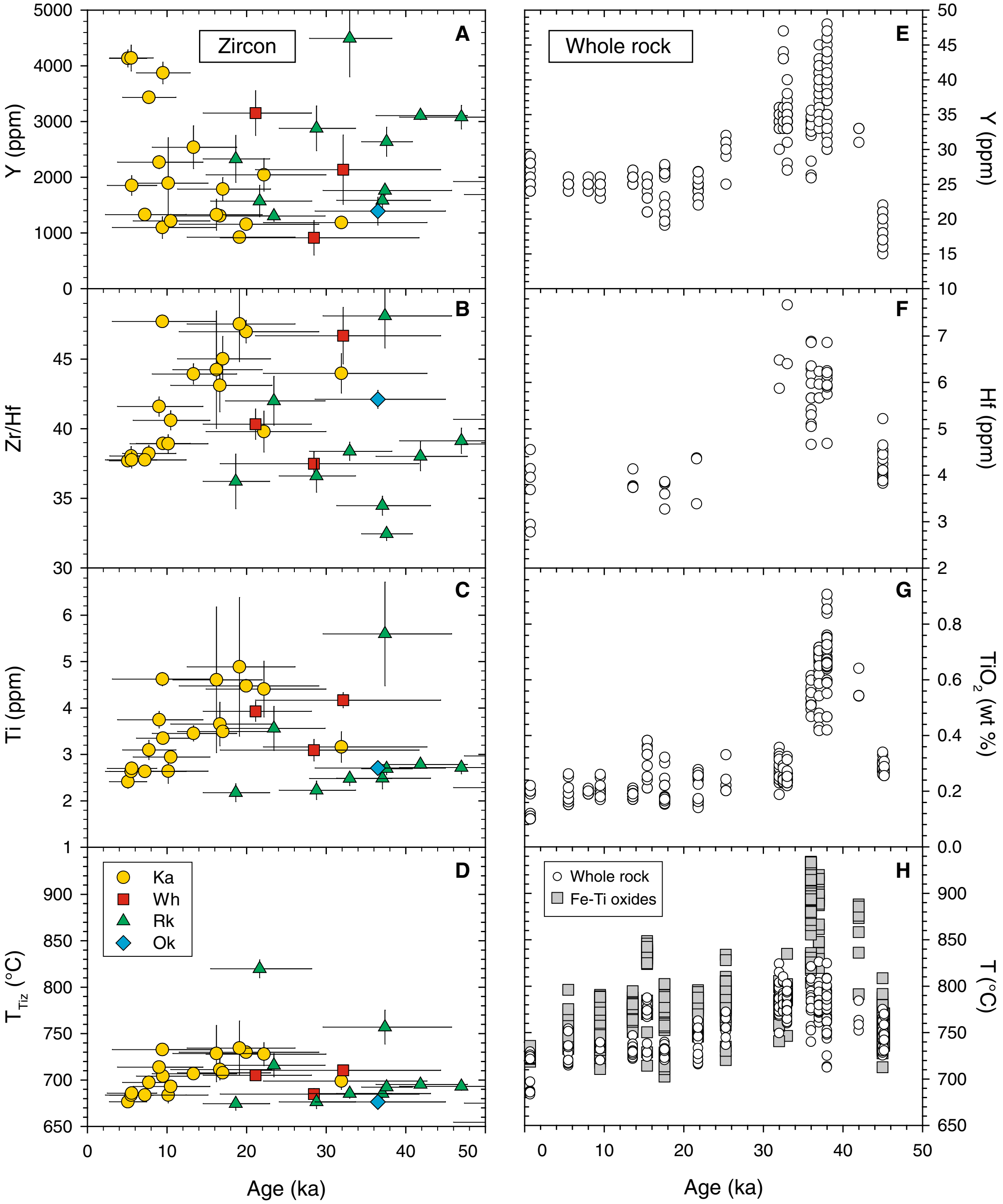

Fig. 10 Zircon compositional and temperature data plotted against crystallization age (*left*) compared to whole rock (zircon saturation temperatures T_{Zrc}) and Fe–Ti oxide thermometry plotted against eruption age (*right*). The whole rock and Fe–Ti data are from Speed et al. (2002); Nairn et al. (2004); Shane et al. (2005b, 2007, 2008a); and Smith et al. (2005). See Fig. 8 caption for details on model T_{Tiz}

The heterogeneous conditions recorded by the dated zircon domains are somewhat reflected in the amphibole record for the post-45 ka history of the OVC (Shane and Smith 2013). Amphibole compositions show that magmas were extracted from reservoirs ranging in *T* between ~700 and 900 °C without systematic variations in magmatic *T* with space or time. This could be interpreted as a large thermally zoned magmatic system buffered from disruptions caused by eruption. The zircon and amphibole thermometers are difficult to compare because of various assumptions in their calibration, intrinsic differences in the time and space of crystallization, and elemental diffusion rates. However, zircon and amphibole re-equilibrate substantially slower than Fe–Ti oxides (e.g., Venezky and

Rutherford 1999) and thus may not record the strong change in compositions and temperatures that is evident from bulk rock and oxide mineral data for rocks erupted immediately after the caldera collapse (Fig. 10).

U–Th disequilibrium dating of Tarawera zircons demonstrates that some co-erupted magmas have disparate crystallization histories on timescales of 10^3–10^4 years (Storm et al. 2011, 2012). Hence, trace element variations should also be distinct for different eruptions. This is borne out in the post-45 ka record (Fig. 10) where zircons from the Kaharoa eruption display a more coherent trend of decreasing Zr/Hf and Ti (and by inference temperature) with time, compared to data from other eruption deposits. This trend could be interpreted as a coherent crystallization and cooling trend from ~20 ka to the time of eruption. Although the zircon data are dominated by Kaharoa, it is important to emphasize that this period essentially encompasses the entire eruption history of Tarawera volcano. The Kaharoa trend thus appears to be continuous despite punctuated eruptions from Tarawera with magma reservoirs and conduit systems in close proximity and in some cases overlapping (Speed et al. 2002; Nairn et al. 2004; Shane et al. 2007, 2008a). As previously noted, the eruption state of the system appears to be dominantly controlled by external factors such as localized mafic intrusion or rifting rather than the crystallinity of the silicic body (Storm et al. 2012). Nevertheless, it is interesting to speculate on the last eruption (AD1886) from Tarawera which was a basaltic plinian event that did not remobilize silicic magma unlike each previous eruption (Shane et al. 2008b). Perhaps the cooling and crystallization trend reflected in the Kaharoa zircons indicates that the system had largely solidified by AD1886 and that this facilitated the rapid ascent of basaltic magma in the youngest eruption of Tarawera.

Conclusion

We introduce high spatial resolution SIMS depth profiling for trace element analysis of zircon by excavating parallel pits into non-polished prism faces to obtain a co-registered age and trace element record. The trace element variations provide high temporal resolution constraints for the chemical and physical state of a long-lived rhyolitic magma system. Zircon micron-scale domains from individual Tarawera eruptive units display significant trace element (Th, U, Y, Ti, Ce, and Zr/Hf) compositional diversity over a ~150 ka period of zircon crystallization. Although rimward depletion in Zr/Hf and Ti is common in many crystals, broadly consistent with cooling and crystallization, occasional reversals of these patterns point to localized magmatic heterogeneity involving magmatic recharge and heating. The diversity of crystals at hand-specimen scale requires considerable transport and mixing prior to eruption and reflects a general lack of homogenization over the entire magmatic system. The compositional diversity is consistent with punctuated and variable crystal growth rates indicated by U–Th disequilibrium dating (Storm et al. 2012). When considered in its entirety, zircon trace element compositions are more heterogeneous subsequent to the ~45 ka caldera-forming eruption, compared to the preceding ~100 ka. About the same time, whole-rock compositions also indicate an excursion to hotter, less evolved magma compositions implying the disruption of an evolving rhyolitic magma system by recharge. Intriguingly, zircon compositional trends during the <45 ka period do not mirror those of the erupted magmas. This is best explained by invoking a compartmentalized intrusive complex for Tarawera volcano and its immediate precursors where small, isolated melt pockets evolved independently. This points to a divergence of subterranean storage conditions where crystal-dominated zones evolve differently than those which generate eruptible magma, resulting in heterogeneous crystal populations, an emerging common characteristic of many crystal populations in arc volcanic rocks (e.g., Claiborne et al. 2010b; Stelten and Cooper 2012). In this sense, zircon crystals are indicators of conditions in a largely crystalline mush, rather than the contemporaneous liquid-dominated magma that feeds volcanic eruptions. The Tarawera zircon data thus support the concept for batholith growth from individually short-lived intrusive pulses that rapidly solidify, cumulatively aggregate into larger bodies, and are only intermittently capable of delivering eruptible magma.

Acknowledgments We thank Oscar Lovera for support in developing probability density plots. Journal reviewers Calvin Miller and Kathryn Watts provided helpful comments. The ion microprobe facility at UCLA is partly supported by a grant from the Instrumentation and Facilities Program, Division of Earth Sciences, National Science Foundation. SSt was supported by a University of Auckland International Doctoral Scholarship, PS by a GNS Science subcontract, and JL by a Fellowship from the New Zealand Earthquake Commission.

References

Bachmann O, Bergantz GW (2004) On the origin of crystal-poor rhyolites: extracted from batholithic crystal mushes. J Petrol 45(8):1565–1582

Bacon CR (1989) Crystallization of accessory phases in magmas by local saturation adjacent to phenocrysts. Geochim Cosmochim Acta 53(5):1055–1066. doi:10.1016/0016-7037(89)90210-X

Bacon CR, Hirschmann M (1988) Mg/Mn partitioning as a test for equilibrium between coexisting Fe–Ti oxides. Am Mineral 73:57–61

Blundy J, Wood B (1994) Prediction of crystal-melt partition coefficients from elastic moduli. Nature 372(6505):452–454. doi:10.1038/372452a0

Blundy J, Wood B (2003) Mineral-melt partitioning of uranium, thorium and their daughters. Rev Mineral Geochem 52(1):59–123. doi:10.2113/0520059

Boehnke P, Watson EB, Trail D, Harrison TM, Schmitt AK (2013) Zircon saturation re-revisited. Chem Geol 351:324–334. doi:10.1016/j.chemgeo.2013.05.028

Charlier BLA, Wilson CJN (2010) Chronology and evolution of caldera-forming and post-caldera magma systems at Okataina Volcano, New Zealand from zircon U–Th model-age spectra. J Petrol 51(5):1121–1141. doi:10.1093/petrology/egq015

Cherniak DJ, Watson EB (2003) Diffusion in zircon. Rev Mineral Geochem 53:113–143

Cherniak DJ, Hanchar JM, Watson EB (1997) Diffusion of tetravalent cations in zircon. Contrib Miner Petrol 127(4):383–390. doi:10.1007/s004100050287

Claiborne LL, Miller CF, Walker BA, Wooden JL, Mazdab FK, Bea F (2006) Tracking magmatic processes through Zr/Hf ratios in rocks and Hf and Ti zoning in zircons: an example from the Spirit Mountain batholith, Nevada. Mineral Mag 70(5):517–543

Claiborne LL, Miller CF, Wooden JL (2010a) Trace element composition of igneous zircon: a thermal and compositional record of the accumulation and evolution of a large silicic batholith, Spirit Mountain, Nevada. Contrib Mineral Petrol 160(4):511–531. doi:10.1007/s00410-010-0491-5

Claiborne LL, Miller CF, Flanagan DM, Clynne MA, Wooden JL (2010b) Zircon reveals protracted magma storage and recycling beneath Mount St. Helens. Geology 38(11):1011–1014

Danišík M, Shane P, Schmitt AK, Hogg A, Santos GM, Storm S, Evans NJ, Fifield KL, Lindsay JM (2012) Re-anchoring the late Pleistocene tephrochronology of New Zealand based on concordant radiocarbon ages and combined 238U/230Th disequilibrium and (U–Th)/He zircon ages. Earth Planet Sci Lett 349–350:240–250. doi:10.1016/j.epsl.2012.06.041

Davidson JP, Morgan DJ, Charlier BLA (2007) Isotopic microsampling of magmatic rocks. Elements 3(4):253–259. doi:10.2113/gselements.3.4.253

Ferry JM, Watson EB (2007) New thermodynamic models and revised calibrations for the Ti-in-zircon and Zr-in-rutile thermometers. Contrib Miner Petrol 154(4):429–437. doi:10.1007/s00410-007-0201-0

Gelman SE, Gutiérrez FJ, Bachmann O (2013) On the longevity of large upper crustal silicic magma reservoirs. Geology 41:759–762. doi:10.1130/g34241.1

Ghiorso MS, Gualda GAR (2012) A method for estimating the activity of titania in magmatic liquids from the compositions of coexisting rhombohedral and cubic iron-titanium oxides. Contrib Miner Petrol. doi:10.1007/s00410-012-0792-y

Ginibre C, Woerner G, Kronz A (2007) Crystal zoning as an archive for magma evolution. Elements 3(4):261–266. doi:10.2113/gselements.3.4.261

Glazner AF, Bartley JM, Coleman DS, Gray W, Taylor RZ (2004) Are plutons assembled over millions of years by amalgamation from small magma chambers? GSA Today 14(4–5):4–11. doi:10.1130/1052-5173(2004)014<0004:APAOMO>2.0.CO;2

Harrison TM, Schmitt AK (2007) High sensitivity mapping of Ti distributions in Hadean zircons. Earth Planet Sci Lett 261(1–2):9–19. doi:10.1016/j.epsl.2007.05.016

Harrison TM, Watson EB, Aikman AB (2007) Temperature spectra of zircon crystallization in plutonic rocks. Geology 35(7):635–638. doi:10.1130/g23505a.1

Hofmann A, Valley J, Watson E, Cavosie A, Eiler J (2009) Sub-micron scale distributions of trace elements in zircon. Contrib Miner Petrol 158(3):317–335. doi:10.1007/s00410-009-0385-6

Holtz F, Johannes W (1994) Maximum and minimum water contents of granitic melts: implications for chemical and physical properties of ascending magmas. Lithos 32(1–2):149–159. doi:10.1016/0024-4937(94)90027-2

Jurado-Chichay Z, Walker GPL (2000) Stratigraphy and dispersal of the Mangaone subgroup pyroclastic deposits, Okataina Volcanic Centre, New Zealand. J Volcanol Geoth Res 104(1–4):319–383. doi:10.1016/S0377-0273(00)00210-9

Klemetti EW, Deering CD, Cooper KM, Roeske SM (2011) Magmatic perturbations in the Okataina Volcanic Complex, New Zealand at thousand-year timescales recorded in single zircon crystals. Earth Planet Sci Lett 305(1–2):185–194. doi:10.1016/j.epsl.2011.02.054

Linnen RL, Keppler H (2002) Melt composition control of Zr/Hf fractionation in magmatic processes. Geochim Cosmochim Acta 66(18):3293–3301. doi:10.1016/S0016-7037(02)00924-9

Liu Y, Hu Z, Zong K, Gao C, Gao S, Xu J, Chen H (2010) Reappraisement and refinement of zircon U–Pb isotope and trace element analyses by LA-ICP-MS. Chin Sci Bull 55(15):1535–1546. doi:10.1007/s11434-010-3052-4

Lowe DJ, Shane PAR, Alloway BV, Newnham RM (2008) Fingerprints and age models for widespread New Zealand tephra marker beds erupted since 30,000 years ago: a framework for NZ-INTIMATE. Quatern Sci Rev 27(1–2):95–126. doi:10.1016/j.quascirev.2007.01.013

Nairn IA (2002) Geology of the Okataina Volcanic Centre: Institute of Geological & Nuclear Sciences Geological Map 25. Lower Hutt, New Zealand, 156 p + 1 sheet

Nairn IA, Kohn BP (1973) Relation of the Earthquake Flat Breccia to the Rotoiti Breccia, central North Island, New Zealand. N Z J Geol Geophys 16:269–279. doi:10.1080/00288306.1973.10431457

Nairn IA, Shane PR, Cole JW, Leonard GJ, Self S, Pearson N (2004) Rhyolite magma processes of the approximately AD 1315 Kaharoa eruption episode, Tarawera Volcano, New Zealand. J Volcanol Geoth Res 131(3–4):265–294. doi:10.1016/S0377-0273(03)00381-0

Reid MR, Coath CD (2000) In situ U–Pb ages of zircons from the Bishop Tuff: no evidence for long crystal residence times. Geology 28(5):443–446

Reid MR, Coath CD, Harrison TM, McKeegan KD (1997) Prolonged residence times for the youngest rhyolites associated with Long Valley Caldera: ^{230}Th–^{238}U ion microprobe dating of young zircons. Earth Planet Sci Lett 150(1–2):27–39. doi:10.1016/S0012-821X(97)00077-0

Reid MR, Vazquez JA, Schmitt AK (2011) Zircon-scale insights into the history of a Supervolcano, Bishop Tuff, Long Valley, California, with implications for the Ti-in-zircon geothermometer. Contrib Miner Petrol 161(2):293–311. doi:10.1007/s00410-010-0532-0

Schmitt AK (2011) Uranium series accessory crystal dating of magmatic processes. Annu Rev Earth Planet Sci 39(1):321–349. doi:10.1146/annurev-earth-040610-133330

Schmitt AK, Perfit MR, Rubin KH, Stockli DF, Smith MC, Cotsonika LA, Zellmer GF, Ridley WI, Lovera OM (2011) Rapid cooling rates at an active mid-ocean ridge from zircon thermochronology. Earth Planet Sci Lett 302(3–4):349–358. doi:10.1016/j.epsl.2010.12.022

Shane P, Smith VC (2013) Using amphibole crystals to reconstruct magma storage temperatures and pressures for the post-caldera collapse volcanism at Okataina volcano. Lithos 156–159:159–170. doi:10.1016/j.lithos.2012.11.008

Shane P, Nairn IA, Smith, VC (2005a) Magma mingling in the ~50 ka Rotoiti eruption from Okataina Volcanic Centre: implications for geochemical diversity and chronology of large volume rhyolites. J Volcanol Geoth Res 139(3–4):295–313. doi:10.1016/j.jvolgeores.2004.08.012

Shane P, Smith VC, Nairn IA (2005b) High temperature rhyodacites of the 36 ka Hauparu pyroclastic eruption, Okataina Volcanic Centre, New Zealand: change in a silicic magmatic system following caldera collapse. J Volcanol Geoth Res 147(3–4):357–376. doi:10.1016/j.jvolgeores.2005.04.015

Shane P, Martin SB, Smith VC, Beggs KF, Darragh MB, Cole JW, Nairn IA (2007) Multiple rhyolite magmas and basalt injection in the 17.7 ka Rerewhakaaitu eruption episode from Tarawera volcanic complex, New Zealand. J Volcanol Geoth Res 164:1–26. doi:10.1016/j.jvolgeores.2007.04.003

Shane P, Nairn IA, Smith VC, Darragh M, Beggs K, Cole JW (2008a) Silicic recharge of multiple rhyolite magmas by basaltic intrusion during the 22.6 ka Okareka eruption episode, New Zealand. Lithos 103(3–4):527–549. doi:10.1016/j.lithos.2007.11.002

Shane P, Smith VC, Nairn I (2008b) Millennial timescale resolution of rhyolite magma recharge at Tarawera volcano: insights from quartz chemistry and melt inclusions. Contrib Miner Petrol 156(3):397–411. doi:10.1007/s00410-008-0292-2

Shane P, Storm S, Schmitt AK, Lindsay JM (2012) Timing and conditions of formation of granitoid clasts erupted in recent pyroclastic deposits from Tarawera Volcano (New Zealand). Lithos 140–141:1–10. doi:10.1016/j.lithos.2012.01.012

Smith VC, Shane P, Nairn IA (2005) Trends in rhyolite geochemistry, mineralogy, and magma storage during the last 50 kyr at Okataina and Taupo volcanic centres, Taupo volcanic zone, New Zealand. J Volcanol Geoth Res 148:372–406. doi:10.1016/j.volgeores.2005.05.005

Speed J, Shane P, Nairn I (2002) Volcanic stratigraphy and phase chemistry of the 11 900 yr BP Waiohau eruptive episode, Tarawera volcanic complex, New Zealand. N Z J Geol Geophys 45(3):395–410

Stelten ME, Cooper KM (2012) Constraints on the nature of the subvolcanic reservoir at South Sister volcano, Oregon from U-series dating combined with sub-crystal trace-element analysis of plagioclase and zircon. Earth Planet Sci Lett 313:1–11

Storm S, Shane P, Schmitt AK, Lindsay JM (2011) Contrasting punctuated zircon growth in two syn-erupted rhyolite magmas from Tarawera volcano: insights to crystal diversity in magmatic systems. Earth Planet Sci Lett 301(3–4):511–520. doi:10.1016/j.epsl.2010.11.034

Storm S, Shane P, Schmitt AK, Lindsay JM (2012) Decoupled crystallization and eruption histories of the rhyolite magmatic system at Tarawera volcano revealed by zircon ages and growth rates. Contrib Miner Petrol 163(3):505–519. doi:10.1007/s00410-011-0682-8

Tappa MJ, Coleman DS, Mills RD, Samperton KM (2011) The plutonic record of a silicic ignimbrite from the Latir volcanic field, New Mexico. Geochem Geophys Geosyst 12(10). doi:10.1029/2011gc003700

Trail D, Watson EB, Tailby ND (2011) The oxidation state of Hadean magmas and implications for early Earth's atmosphere. Nature 480(7375):79–82

Venezky DY, Rutherford MJ (1999) Petrology and Fe–Ti oxide reequilibration of the 1991 Mount Unzen mixed magma. J Volcanol Geoth Res 89(1–4):213–230. doi:10.1016/S0377-0273(98)00133-4

Watson EB (1996) Dissolution, growth and survival of zircons during crustal fusion: kinetic principles, geological models and implications for isotopic inheritance. Spec Pap Geol Soc Am 315:43–56. doi:10.1130/0-8137-2315-9.43

Watson EB, Harrison TM (1983) Zircon saturation revisited: temperature and composition effects in a variety of crustal magma types. Earth Planet Sci Lett 64(2):295–304. doi:10.1016/0012-821X(83)90211-X

Wilson CJN, Gravley DM, Leonard GS, Rowland JV (2009) Volcanism in the central Taupo volcanic zone, New Zealand: tempo, styles and controls. Spec Publ Int Assoc Volcanol Chem Earth's Inter 2:225–247

Zimmerer MJ, McIntosh WC (2012) The geochronology of volcanic and plutonic rocks at the Questa caldera: constraints on the origin of caldera-related silicic magmas. Geol Soc Am Bull 124:1394–1408. doi:10.1130/b30544.1